

Nonlinear Mode Coupling in Silicon Nitride Membrane Resonators

Soumya Kanti Das^{*,1}, Nishta Arora^{*†,2}, Hridhay A S,¹ Akshay Naik,² and Chandan Samanta^{‡1}

¹*Department of Physics,*

Indian Institute of Science Education and Research Bhopal, Bhopal-462066, Madhya Pradesh, India

²*Centre for Nano Science and Engineering,*

Indian Institute of Science, Bengaluru-560012, Karnataka, India

Nonlinear interactions between vibrational modes play a crucial role in understanding the dynamical response of nanomechanical resonators. Here, we report the experimental observation and theoretical modeling of nonlinear mode coupling in a high-stress square silicon nitride membrane resonator. We quantify frequency shifts of the fundamental mode arising from tension-mediated geometric nonlinearity by increasing the amplitude of the fundamental mode and higher-order flexural modes. A quantitative theoretical framework based on Kirchhoff–Love plate theory is developed, which incorporates both intrinsic Duffing nonlinearity and nonlinear intermodal coupling and shows good agreement with experimental measurements for the (1,1)-(2,1) and (1,1)-(2,2) mode pairs. We further compute the nonlinear coupling matrix across mode families, revealing the role of mode symmetry and spatial overlap in governing intermodal interactions. These results establish nonlinear mode coupling as a controllable resource for multimode frequency tuning and mechanical transduction.

Mechanical resonators[1, 2] play an important role in both fundamental research and emerging technologies. Their exceptional sensitivity to external stimuli underpins advances across a wide range of research areas, including force sensing[3–5], mass spectrometry[6, 7], magnetometry[8–11], accelerometers[12, 13], pressure sensors[14–16], magnetic resonance imaging[17–19], and scanning probe microscopy[20, 21]. Beyond sensing, mechanical resonators are widely used in communications and signal processing[22–24]. They serve as key interfaces in hybrid quantum systems[25, 26], coupling mechanical motion to optical[27, 28], electrical[29, 30], and spin[31–33] degrees of freedom. These capabilities establish mechanical resonators as a unifying platform bridging classical and quantum physics[34–37], combining technological relevance with fundamental discovery[38, 39].

Among various classes of mechanical resonators, high-stress silicon nitride (Si_3N_4) membranes have emerged as a leading platform. Their resonance frequencies, quality factor, and mechanical mode shapes can be precisely engineered through device geometry and boundary conditions. Their exceptionally high quality factors[40–45] and compatibility with chip-scale integration make these resonators well suited for precision sensing and for probing mechanical dynamics at room and cryogenic temperatures[46, 47]. As a result, these resonators are playing an increasingly important role in exploring light-matter interaction[48, 49], ground state cooling[50], entanglement[51], optomechanical squeezing[52], optical-to-microwave photon transducers[53], quantum memory[54], gravitational-wave detection[55], dark matter detector[56], and advanced precision sensing[57].

Most studies of Si_3N_4 membrane resonators have focused on single, isolated vibrational modes [58–60],

whereas practical membranes support a dense spectrum of mechanical resonances whose interactions can strongly influence device dynamics and performance. At sufficiently large oscillation amplitudes, mechanical resonators enter into a nonlinear regime governed by tension-induced geometric nonlinearity, enabling nonlinear modal coupling that gives rise to amplitude-dependent frequency tuning, energy exchange between orthogonal modes, and dynamic control of the mechanical response[61]. These effects enable multimode functionalities including hybridized resonances[62, 63], enhanced energy transfer[64, 65], bandwidth broadening [66], and tunable dissipation pathways [67–69]. Despite their importance, nonlinear modal interactions in square Si_3N_4 membranes remain largely unexplored, even though they are crucial for advanced sensing, signal processing, and hybrid classical–quantum transduction architectures.

In this work, we present an experimental and theoretical study of nonlinear intra- and intermodal coupling in a high-stress square Si_3N_4 membrane resonator. By driving multiple flexural modes into the nonlinear regime, we observe amplitude-dependent frequency shifts arising from both intramodal (intrinsic Duffing nonlinearity) and intermodal coupling. We develop a simple yet quantitative theoretical framework based on Kirchhoff–Love plate theory that accurately captures these effects. Through a systematic mapping of coupling strengths across mode families, we compute the coupling matrix between the fundamental and higher-order modes, revealing the role of modal overlap in governing nonlinear interactions. Furthermore, we compute the selective frequency tuning of a target mode via the excitation of orthogonal modes, establishing nonlinear mode coupling as a powerful resource for engineering multimode functionality in high-

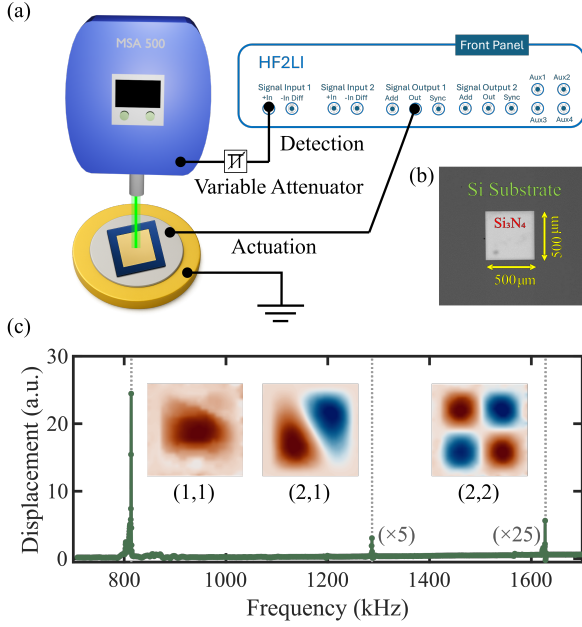


Fig. 1. Measurement setup and vibrational modes of the device. (a) Schematic of the laser Doppler vibrometry (LDV) based measurement setup. A Polytec MSA-500 system is used to optically probe the out-of-plane motion of Si_3N_4 membrane, while electrical actuation and signal detection are performed using a Zurich instruments HF2LI lock-in amplifier. (b) Optical micrograph of the device, showing a $500\ \mu\text{m} \times 500\ \mu\text{m}$ Si_3N_4 membrane suspended over a silicon substrate. (c) Measured displacement amplitude spectrum with drive frequency showing multiple mechanical resonances. Higher frequency modes are scaled by a factor of $\times 5$ and $\times 25$ for visibility. Inset shows the corresponding spatial mode shapes of the resonant modes.

stress Si_3N_4 membrane resonators.

The experiments are performed on a suspended silicon nitride square membrane from Norcada with side length (L) of $500\ \mu\text{m}$ and a thickness (h) of $100\ \text{nm}$ clamped to a $500\ \mu\text{m}$ thick silicon substrate. The $\text{Si}_3\text{N}_4/\text{Si}$ substrate is mounted on a piezoelectric actuator that enables out-of-plane excitation via an applied AC voltage $V(t) = V_0 \cos(\omega t)$. The frequency-amplitude response of the membrane is measured optically using a laser Doppler vibrometer (Polytec MSA 500). All measurements were performed under high vacuum at a base pressure of 2×10^{-5} mbar to minimize air damping. Figure 1(a) shows a schematic of the experimental setup, in which a lock-in amplifier (Zurich Instruments HF2LI) is used to simultaneously actuate and detect the mechanical motion of the membrane. An optical micrograph of the membrane and the measured mode spectrum between 700 and 1700 kHz are presented in Figs. 1(b) and 1(c), respectively. Three vibrational modes are observed within this frequency range; the inset shows the measured spatial mode shapes, with modes labeled (n, m) according to the number of anti-nodes along the two in-plane

directions of the membrane.

We first characterize the out-of-plane vibrational modes at low drive amplitudes, where both intramodal and intermodal coupling are negligible. Figure 2(b) shows the linear frequency response of the (1,1) mode, while the responses of the (2,1) and (2,2) modes are presented in Fig. S4. In this regime, all modes exhibit Lorentzian line shapes. The measured resonance frequencies of the (1,1), (2,1), and (2,2) modes are 814 kHz, 1286 kHz, and 1628 kHz, with corresponding quality factors of 5.2×10^4 , 12.5×10^4 , and 11.3×10^4 , respectively. Figure 2(a) displays the nonlinear frequency response of the (1,1) mode, measured at increasing drive amplitudes, arising from intrinsic Duffing nonlinearity.

We describe the membrane dynamics within the framework of Kirchhoff–Love plate theory[70]. The transverse displacement $w(x, y, t)$ satisfies

$$D\nabla^4 w(x, y, t) - \left(N_{xx} \frac{\partial^2 w}{\partial x^2} + 2N_{xy} \frac{\partial^2 w}{\partial x \partial y} + N_{yy} \frac{\partial^2 w}{\partial y^2} \right) + \rho h \frac{\partial^2 w}{\partial t^2} = 0, \quad (1)$$

where D is the flexural rigidity, N_{xx}, N_{xy}, N_{yy} are the in-plane stress resultants, ρ is the mass density of the membrane and h is the thickness. Within the high stressed thin membrane approximation[71] the in-plane stress components can be expressed as

$$\begin{aligned} N_{xx} &= Eh \left(\epsilon_0 + \frac{1}{2} \left(\frac{\partial w}{\partial x} \right)^2 \right), \\ N_{yy} &= Eh \left(\epsilon_0 + \frac{1}{2} \left(\frac{\partial w}{\partial y} \right)^2 \right), \\ N_{xy} &= \frac{1}{2} Eh \left(\frac{\partial w}{\partial x} \frac{\partial w}{\partial y} \right), \end{aligned} \quad (2)$$

where E is the Young's modulus, and ϵ_0 is the built-in tensile strain of the membrane. The transverse displacement is expressed as $w(x, y, t) = \phi(x, y) z(t)$, where $\phi(x, y) = \sin\left(\frac{n\pi x}{L}\right) \sin\left(\frac{m\pi y}{L}\right)$ is the spatial mode shape and $z(t)$ is the corresponding out of plane displacement. Substituting the mode expansion into Eq. (1) and applying the Galerkin discretizations procedure, followed by the inclusion of linear damping (ν) and external driving force ($f_d \cos(\omega_d t)$), yields the Duffing equation of motion

$$\ddot{z} + \omega_{nm}^2 z + \nu \dot{z} + \alpha_{nm} z^3 = f_d \cos(\omega_d t), \quad (3)$$

The expressions for the linear resonance frequency ω_{nm} and the Duffing coefficient α_{nm} for a general mode (n, m) are given by

$$\omega_{nm}^2 = \frac{E\epsilon_0\pi^2(n^2 + m^2)}{\rho L^2}, \quad (4)$$

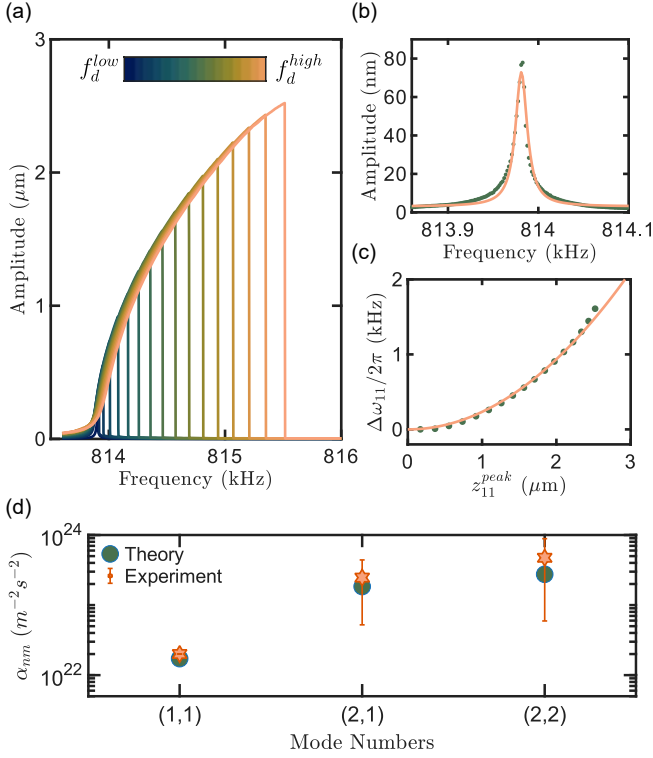


Fig. 2. Intramodal coupling and Duffing constant. (a) Nonlinear frequency response of the (1,1) mode, measured at increasing drive strengths. (b) Linear response of the (1,1) mode at the lowest drive amplitude; solid lines indicate Lorentzian fits used to extract the resonance frequency and quality factor. (c) Amplitude-dependent frequency shift corresponding to the maximum displacement amplitudes extracted from (a). Solid line show fit using Eq. (6) to extract the Duffing coefficient. (d) Comparison of the experimentally extracted Duffing coefficients with theoretical values calculated from Eq. (5) for the (1,1), (2,1), and (2,2) modes.

$$\alpha_{nm} = \frac{3E}{32\rho} \left(\frac{\pi}{L}\right)^4 \left[n^4 + m^4 - \frac{2}{3}n^2m^2\right]. \quad (5)$$

We use the measured resonance frequency of the fundamental (1,1) mode to extract the built-in tensile strain $\epsilon_0 = 3.7 \times 10^{-3}$ from Eq. (4). This value is subsequently used to estimate the theoretical resonance frequencies of higher-order modes, shown by the dashed lines in Fig. 1(c), which are in good agreement with the experimentally observed higher mode frequencies. Solving Eq. (3) using the method of multiple scales yields an amplitude-dependent nonlinear pulling of the resonance frequency,

$$\omega_{nm}^{peak} = \omega_{nm} + \frac{3\alpha_{nm}}{8\omega_{nm}} (z^{peak})^2, \quad (6)$$

where z^{peak} denotes the maximum displacement amplitude of the (n,m) mode. The measured values of z^{peak} is plotted as a function of the shift in peak frequency

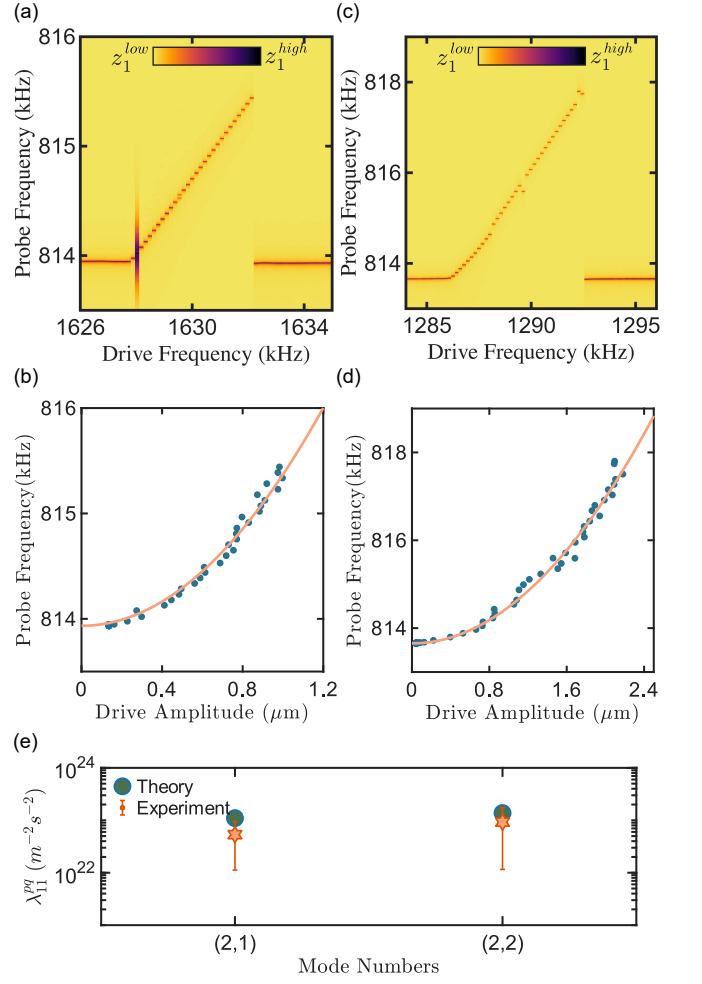


Fig. 3. Nonlinear intermodal coupling. (a,c) Resonance frequency-shifting phenomena of the fundamental (1,1) mode induced by strong excitation of the (2,2) and (2,1) modes, respectively. (b,d) Extracted resonance frequency of the (1,1) mode as a function of the displacement amplitude of the driven (2,2) and (2,1) modes, respectively. Solid lines represent fits to the data using Eq. (9) to extract the nonlinear intermodal coupling constants. (e) Comparison of experimentally extracted coupling constants (stars) with theoretical values (circles) calculated from Eq. S40.

($\omega_{nm}^{peak} - \omega_{nm}$) for the (1,1) mode in Fig. 2(c). The data is fitted using Eq. (6), with Duffing constant as the sole free parameter. The experimental Duffing coefficients for the (1,1), (2,1), and (2,2) modes are extracted and found to be $2 \times 10^{22} \text{ m}^{-2}\text{s}^{-2}$, $2.5 \times 10^{23} \text{ m}^{-2}\text{s}^{-2}$, and $4.7 \times 10^{23} \text{ m}^{-2}\text{s}^{-2}$, respectively. Figure 2(d) shows good agreement between the experimentally obtained Duffing coefficients and the theoretical values calculated from Eq. (5). The corresponding analysis for the (2,1) and (2,2) modes are presented in Fig. S4 of the Supplementary Material.

When a higher order mode is driven into the nonlinear regime, its large amplitude oscillation modifies the tensile stress of the membrane. This displacement-dependent tension acts as an effective parametric perturbation for

other modes, leading to nonlinear intermodal coupling. As a result the resonance frequency of the fundamental mode becomes dependent on the oscillation amplitude of the driven higher-order mode. To experimentally probe this effect, we strongly drive the (2, 1) and (2, 2) modes near their resonance frequencies while simultaneously monitoring the response of the fundamental (1, 1) mode using a weak probe tone. Figures 3(a) and 3(c) show color plots of the fundamental-mode response as a function of probe frequency and drive frequency applied to the higher-order modes. A clear amplitude-dependent frequency shift of the (1, 1) mode is observed, indicative of nonlinear frequency pulling due to intermodal coupling. The localized enhancement in spectral amplitude of the fundamental mode observed near a drive frequency ~ 1628 kHz in Fig. 3(a) arises from a subharmonic component of the drive signal. This feature is absent in Fig. 3(c), where such harmonic components are not resonant with the fundamental mode.

In order to theoretically evaluate the intermodal coupling constant, we modify the in-plane stress component as

$$\begin{aligned} N_{xx} &= Eh \left[\epsilon_0 + \frac{1}{2} \left\{ \left(\frac{\partial w_1}{\partial x} \right)^2 + \left(\frac{\partial w_2}{\partial x} \right)^2 \right\} \right], \\ N_{yy} &= Eh \left[\epsilon_0 + \frac{1}{2} \left\{ \left(\frac{\partial w_1}{\partial y} \right)^2 + \left(\frac{\partial w_2}{\partial y} \right)^2 \right\} \right], \\ N_{xy} &= \frac{1}{2} Eh \left[\left(\frac{\partial w_1}{\partial x} \frac{\partial w_1}{\partial y} \right) + \left(\frac{\partial w_2}{\partial x} \frac{\partial w_2}{\partial y} \right) \right], \end{aligned} \quad (7)$$

where $w_1 = \sin(\frac{n\pi x}{L}) \sin(\frac{m\pi y}{L}) z_1(t)$ and $w_2 = \sin(\frac{p\pi x}{L}) \sin(\frac{q\pi y}{L}) z_2(t)$ represent the transverse displacements of the probing and driving modes, respectively. Substituting the mode shapes into the governing plate equation and applying the Galerkin discretization procedure, followed by the inclusion of linear damping (ν_1) and external probing force ($f_p \cos(\omega_p t)$) terms, yields the probe mode equation of motion as

$$\ddot{z}_1 + \omega_{nm}^2 z_1 + \nu_1 \dot{z}_1 + \alpha_{nm} z_1^3 + \lambda_{nm}^{pq} z_1 z_2^2 = f_p \cos(\omega_p t), \quad (8)$$

where λ_{nm}^{pq} represents the coupling constant between the driving mode (p, q) and the probing mode (n, m). Applying the method of multiple scales to Eq. (8), we obtain the effective resonance frequency of the fundamental mode arising from intermodal coupling as

$$\omega = \omega_{nm} + \frac{3\alpha_{nm}}{8\omega_{nm}} (z_1^{peak})^2 + \frac{\lambda_{nm}^{pq}}{2\omega_{nm}} z_2^2, \quad (9)$$

where z_2 is the amplitude of the driven higher order mode. The experimentally measured frequency shifts are shown in Figs. 3(b) and 3(d). The data are fitted using Eq. (9), with λ_{nm}^{pq} as the sole fitting parameter. From these fits, we extract the intermodal coupling constants

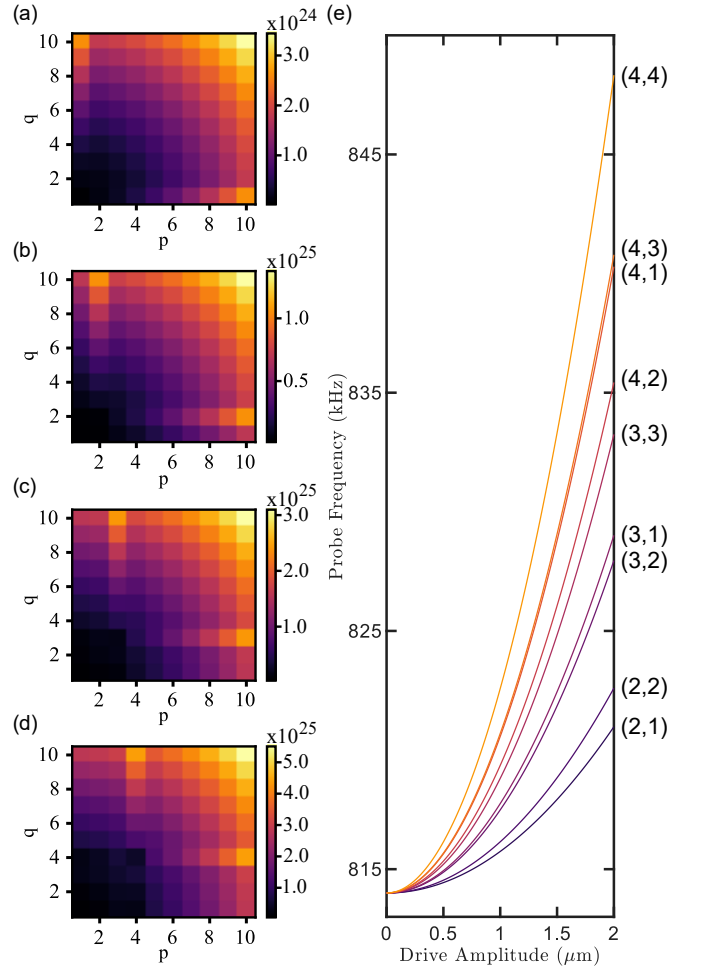


Fig. 4. Theoretical estimation of the nonlinear mode coupling matrix. (a–d) Calculated coupling constants as a function of the driven mode indices (p, q) for $p, q = 1-10$, coupled to the probe modes (1, 1), (2, 2), (3, 3), and (4, 4), respectively. (e) Predicted frequency shift of the fundamental mode as a function of the coupled-mode amplitude, calculated using the theoretical coupling constants listed in Table I.

for the (1, 1)–(2, 1) and (1, 1)–(2, 2) mode pairs, yielding values of $5.3 \times 10^{22} \text{ m}^{-2} \text{ s}^{-2}$ and $9.2 \times 10^{22} \text{ m}^{-2} \text{ s}^{-2}$, respectively. As shown in Fig. 3(e), the extracted coupling constants are in good agreement with the theoretical predictions obtained from Eq. S40. At very high drive amplitudes, the model breaks down due to the onset of higher-order nonlinearities in the driven mode, which modify the standard Duffing response[66, 72].

Using the Kirchhoff-Love plate theory, we further compute the nonlinear coupling constants between the fundamental mode and higher-order modes using Eq. S40. We first consider the probe mode with $n = m$. Figure 4(a–d) shows the variation of the coupling constant as the driven mode indices (p, q) are varied from 1 to 10, while the probe modes are fixed at (1, 1), (2, 2), (3, 3), and (4, 4), respectively. For driven modes with $p, q \neq n$, the coupling constant λ_{nm}^{pq} increases monotonically with

TABLE I. This table shows the value of coupling constant per unit modal mass for different modes with mode number (p,q) , which is coupled to $(1,1)$ mode. All the values here are of the order $10^{23} m^{-2} s^{-2}$. The intramode coupling constant (Duffing constant) is highlighted in blue.

| | $q = 1$ | $q = 2$ | $q = 3$ | $q = 4$ |
|---------|-------------|---------|---------|---------|
| $p = 1$ | 0.17 | 1.12 | 2.41 | 4.22 |
| $p = 2$ | 1.12 | 1.38 | 2.24 | 3.44 |
| $p = 3$ | 2.41 | 2.24 | 3.09 | 4.30 |
| $p = 4$ | 4.22 | 3.44 | 4.30 | 5.51 |

increasing p or q when the other index is held fixed. In the special case $p = n$ or $q = m$, λ_{nm}^{pq} exhibits a sharp increase with increasing p or q , respectively, due to enhanced mode overlap. When $n = m = p = q$, λ_{nm}^{pq} reduces to intramodal coupling and equals the Duffing constant of the mode. For probe modes with $n \neq m$, the symmetry is broken (see Supplementary Fig. S1). In this case, λ_{nm}^{pq} exhibits a sharp increase when either $p = n$ or $q = m$. When $n < m$, the coupling constant λ_{nm}^{pq} is larger for $p = n$ than for $q = m$. Conversely, when $m < n$, λ_{nm}^{pq} is larger for $q = m$ than for $p = n$. When $p = n$ and $q = m$ then λ_{nm}^{pq} again reduces to the intramodal coupling constant. The calculated coupling parameters for mode indices $p, q = 1-4$, shown in Fig. 4(a), are listed in Table I. The coupling matrix exhibits clear symmetry with respect to the mode indices and reveals a systematic increase in coupling strength for higher-order modes, as discussed above. Using the coupling parameters in Table I, we predict the frequency shift of the fundamental mode as a function of the coupled-mode amplitude, as shown in Fig. 4(e). These results highlight nonlinear intermodal coupling as an effective mechanism for frequency control.

In conclusion, we experimentally demonstrate and quantitatively model nonlinear intra- and intermodal coupling in a high-stress silicon nitride membrane resonator arising from tension induced geometric nonlinearity. By independently driving selected flexural modes into the nonlinear regime, we directly measure amplitude-dependent frequency shifts originating from intrinsic Duffing nonlinearity as well as from nonlinear coupling between orthogonal modes. Using a Kirchhoff–Love plate theory framework, we derived expressions for the Duffing and intermodal coupling coefficients and showed quantitative agreement with experimental measurements for multiple mode pairs, including the $(1,1)$ - $(2,1)$ and $(1,1)$ - $(2,2)$ interactions. Beyond individual mode pairs, we computed the full nonlinear coupling matrix across mode families, explicitly demonstrating how mode symmetry and spatial overlap determine the magnitude and selectivity of intermodal interactions. These results establish nonlinear mode coupling in Si_3N_4 membranes as a predictable and controllable mechanism for

frequency tuning and multimode transduction. The presented framework provides a direct route to engineering mechanical responses in membrane resonators, with immediate implications for multimode sensing, mechanically mediated signal processing, and hybrid opto- and electro-mechanical systems where controlled mode interactions are essential[62, 73–75].

-
- [1] Adrian Bachtold, Joel Moser, and MI Dykman. Mesoscopic physics of nanomechanical systems. *Reviews of Modern Physics*, 94(4):045005, 2022.
 - [2] Bo Xu, Pengcheng Zhang, Jiankai Zhu, Zuheng Liu, Alexander Eichler, Xu-Qian Zheng, Jaesung Lee, Aneesh Dash, Swapnil More, Song Wu, et al. Nanomechanical resonators: toward atomic scale. *Acs Nano*, 16(10):15545–15585, 2022.
 - [3] HJ Mamin and D Rugar. Sub-attoneutron force detection at millikelvin temperatures. *Applied Physics Letters*, 79(20):3358–3360, 2001.
 - [4] Emanuel Gavartin, Pierre Verlot, and Tobias J Kippenberg. A hybrid on-chip optomechanical transducer for ultrasensitive force measurements. *Nature nanotechnology*, 7(8):509–514, 2012.
 - [5] SL De Bonis, C Urgell, W Yang, C Samanta, Adrien Noury, J Vergara-Cruz, Q Dong, Y Jin, and Adrian Bachtold. Ultrasensitive displacement noise measurement of carbon nanotube mechanical resonators. *Nano letters*, 18(8):5324–5328, 2018.
 - [6] Akshay K Naik, MS Hanay, WK Hiebert, XL Feng, and Michael L Roukes. Towards single-molecule nanomechanical mass spectrometry. *Nature nanotechnology*, 4(7):445–450, 2009.
 - [7] Sergio Dominguez-Medina, Shawn Fostner, Martial Defoort, Marc Sansa, Ann-Kathrin Stark, Mohammad Abdul Halim, Emeline Vernhes, Marc Gely, Guillaume Jourdan, Thomas Alava, et al. Neutral mass spectrometry of virus capsids above 100 megadaltons with nanomechanical resonators. *Science*, 362(6417):918–922, 2018.
 - [8] S Forstner, S Prams, J Knittel, ED Van Ooijen, JD Swaim, GI Harris, A Szorkovszky, WP Bowen, and H Rubinsztein-Dunlop. Cavity optomechanical magnetometer. *Physical review letters*, 108(12):120801, 2012.
 - [9] N Rossi, B Gross, Florian Dirnberger, Dominique Bougeard, and M Poggio. Magnetic force sensing using a self-assembled nanowire. *Nano letters*, 19(2):930–936, 2019.
 - [10] Makars Šiškins, Martin Lee, Samuel Mañas-Valero, Eugenio Coronado, Yaroslav M Blanter, Herre SJ van der Zant, and Peter G Steeneken. Magnetic and electronic phase transitions probed by nanomechanical resonators. *Nature communications*, 11(1):2698, 2020.
 - [11] SM Enamul Hoque Yousuf, Yunong Wang, Shreyas Ramachandran, John Koptur-Palenchar, Chiara Tarantini, Li Xiang, Stephen McGill, Dmitry Smirnov, Elton JG Santos, Philip X-L Feng, et al. Mechanical resonant sensing of spin texture dynamics in a 2d antiferromagnet. *Advanced Materials*, page 2420168, 2025.
 - [12] Alexander G Krause, Martin Winger, Tim D Blasius, Qiang Lin, and Oskar Painter. A high-resolution mi-

- crochip optomechanical accelerometer. *Nature Photonics*, 6(11):768–772, 2012.
- [13] Nathaniel Bawden, Benjamin J Carey, Poh-Meng Yeo, Nishta Arora, Leo Sementilli, Victor M Valenzuela, Erick Romero, Glen I Harris, Margaret Wegener, and Warwick P Bowen. Precision optomechanical accelerometer via hybrid test-mass integration. *Physical Review Applied*, 24(6):064008, 2025.
- [14] Christoph Reinhardt, Hossein Masalehdan, Sandy Croatto, Alexander Franke, Moritz BK Kunze, Jorn Schaffran, Nils Sültmann, Axel Lindner, and Roman Schnabel. Self-calibrating gas pressure sensor with a 10-decade measurement range. *ACS photonics*, 11(4):1438–1446, 2024.
- [15] Olivia R Green, Yiliang Bao, John R Lawall, Jason J Gorman, and Daniel S Barker. Accurate, precise pressure sensing with tethered optomechanics. *Physical Review Applied*, 24(2):024069, 2025.
- [16] Yanping Chen, Shen Liu, Guiqing Hong, Mengqiang Zou, Bonan Liu, Junxian Luo, and Yiping Wang. Nano-optomechanical resonators for sensitive pressure sensing. *ACS Applied Materials & Interfaces*, 14(34):39211–39219, 2022.
- [17] Martino Poggio and Christian L Degen. Force-detected nuclear magnetic resonance: recent advances and future challenges. *Nanotechnology*, 21(34):342001, 2010.
- [18] CL Degen, M Poggio, HJ Mamin, CT Rettner, and D Rugar. Nanoscale magnetic resonance imaging. *Proceedings of the National Academy of Sciences*, 106(5):1313–1317, 2009.
- [19] Urs Grob, Marc-Dominik Krass, M Héritier, Raphael Pachlatko, Jan Rhensius, Jan Kosata, BA Moores, H Takahashi, Alexander Eichler, and Christian L Degen. Magnetic resonance force microscopy with a one-dimensional resolution of 0.9 nanometers. *Nano letters*, 19(11):7935–7940, 2019.
- [20] Laure Mercier De Lépinay, Benjamin Pigeau, Benjamin Besga, Pascal Vincent, Philippe Poncharal, and Olivier Arcizet. A universal and ultrasensitive vectorial nanomechanical sensor for imaging 2d force fields. *Nature nanotechnology*, 12(2):156–162, 2017.
- [21] Nicola Rossi, Floris R Braakman, Davide Cadeddu, Denis Vasyukov, Gözde Tütüncüoğlu, Anna Fontcuberta i Morral, and Martino Poggio. Vectorial scanning force microscopy using a nanowire sensor. *Nature nanotechnology*, 12(2):150–155, 2017.
- [22] I Mahboob, E Flurin, K Nishiguchi, A Fujiwara, and H Yamaguchi. Interconnect-free parallel logic circuits in a single mechanical resonator. *Nature communications*, 2(1):198, 2011.
- [23] Erick Romero, Nicolas P Mauranyapin, Timothy MF Hirsch, Rachpon Kalra, Christopher G Baker, Glen I Harris, and Warwick P Bowen. Acoustically driven single-frequency mechanical logic. *Physical Review Applied*, 21(5):054029, 2024.
- [24] Ce Zhang, Heng Lu, Chen Yang, YuBin Zhang, FengNan Chen, Ying Yan, and Joel Moser. A few-layer graphene nanomechanical resonator driven by multifrequency digital signals. *Nature Communications*, 2025.
- [25] Gershon Kurizki, Patrice Bertet, Yuimaru Kubo, Klaus Mølmer, David Petrosyan, Peter Rabl, and Jörg Schmiedmayer. Quantum technologies with hybrid systems. *Proceedings of the National Academy of Sciences*, 112(13):3866–3873, 2015.
- [26] AA Clerk, KW Lehnert, P Bertet, JR Petta, and Y Nakamura. Hybrid quantum systems with circuit quantum electrodynamics. *Nature Physics*, 16(3):257–267, 2020.
- [27] Shabir Barzanjeh, André Xuereb, Simon Gröblacher, Mauro Paternostro, Cindy A Regal, and Eva M Weig. Optomechanics for quantum technologies. *Nature Physics*, 18(1):15–24, 2022.
- [28] Yiwen Chu and Simon Gröblacher. A perspective on hybrid quantum opto-and electromechanical systems. *Applied Physics Letters*, 117(15), 2020.
- [29] A Naik, O Buu, MD LaHaye, AD Armour, AA Clerk, MP Blencowe, and KC Schwab. Cooling a nanomechanical resonator with quantum back-action. *Nature*, 443(7108):193–196, 2006.
- [30] Carlos Urgell, Wei Yang, Sergio Lucio De Bonis, Chandan Samanta, Maria José Esplandiú, Quan Dong, Yong Jin, and Adrian Bachtold. Cooling and self-oscillation in a nanotube electromechanical resonator. *Nature Physics*, 16(1):32–37, 2020.
- [31] Daniel Rugar, Raffi Budakian, HJ Mamin, and BW Chui. Single spin detection by magnetic resonance force microscopy. *Nature*, 430(6997):329–332, 2004.
- [32] Rodrigo A Thomas, Michał Parniak, Christoffer Østfeldt, Christoffer B Møller, Christian Bærentsen, Yeghishe Tsaturyan, Albert Schliesser, Jürgen Appel, Emil Zeuthen, and Eugene S Polzik. Entanglement between distant macroscopic mechanical and spin systems. *Nature Physics*, 17(2):228–233, 2021.
- [33] Federico Fedele, Federico Cerisola, Lea Bresque, Florian Vigneau, Juliette Monsel, Jorge Tabanera-Bravo, Kushagra Aggarwal, Jonathan Dexter, Sofia Sevitz, Joe Dunlop, et al. Coupling a single spin to the motion of a carbon nanotube. *Nature Communications*, 2025.
- [34] John D Teufel, Tobias Donner, Dale Li, Jennifer W Harlow, MS Allman, Katarina Cicak, Adam J Sirois, Jed D Whittaker, Konrad W Lehnert, and Raymond W Simmonds. Sideband cooling of micromechanical motion to the quantum ground state. *Nature*, 475(7356):359–363, 2011.
- [35] E Alex Wollack, Agnetta Y Cleland, Rachel G Grunenke, Zhaoyou Wang, Patricio Arrangoiz-Arriola, and Amir H Safavi-Naeini. Quantum state preparation and tomography of entangled mechanical resonators. *Nature*, 604(7906):463–467, 2022.
- [36] C Samanta, SL De Bonis, CB Møller, R Tormo-Queralt, W Yang, C Urgell, B Stamenic, B Thibeault, Y Jin, DA Czaplewski, et al. Nonlinear nanomechanical resonators approaching the quantum ground state. *Nature Physics*, 19(9):1340–1344, 2023.
- [37] Yu Yang, Igor Kladarić, Maxwell Drimmer, Uwe von Lüpke, Daan Lenterman, Joost Bus, Stefano Marti, Matteo Fadel, and Yiwen Chu. A mechanical qubit. *Science*, 386(6723):783–788, 2024.
- [38] William M Campbell, Ben T McAllister, Maxim Goryachev, Eugene N Ivanov, and Michael E Tobar. Searching for scalar dark matter via coupling to fundamental constants with photonic, atomic, and mechanical oscillators. *Physical review letters*, 126(7):071301, 2021.
- [39] J Manley, CA Condos, S Schlamminger, JR Pratt, DJ Wilson, and WA Terrano. Microscale torsion resonators for short-range gravity experiments. *Physical Review D*, 110(12):122005, 2024.
- [40] Yeghishe Tsaturyan, Andreas Barg, Eugene S Polzik, and Albert Schliesser. Ultracoherent nanomechanical res-

- onators via soft clamping and dissipation dilution. *Nature nanotechnology*, 12(8):776–783, 2017.
- [41] Mingyun Yuan, Martijn A Cohen, and Gary A Steele. Silicon nitride membrane resonators at millikelvin temperatures with quality factors exceeding 108. *Applied Physics Letters*, 107(26), 2015.
- [42] S Chakram, YS Patil, L Chang, and M Vengalattore. Dissipation in ultrahigh quality factor silicon membrane resonators. *Physical review letters*, 112(12):127201, 2014.
- [43] Xingchen Ji, Samantha Roberts, Mateus Corato-Zanarella, and Michal Lipson. Methods to achieve ultrahigh quality factor silicon nitride resonators. *APL Photonics*, 6(7), 2021.
- [44] Nils Johan Engelsen, Alberto Beccari, and Tobias Jan Kippenberg. Ultrahigh-quality-factor micro-and nanomechanical resonators using dissipation dilution. *Nature Nanotechnology*, 19(6):725–737, 2024.
- [45] Xiang Xi, Iliia Chernobrovkin, Jan Kořata, Mads B Kristensen, Eric Langman, Anders S Sørensen, Oded Zilberberg, and Albert Schliesser. A soft-clamped topological waveguide for phonons. *Nature*, pages 1–7, 2025.
- [46] TP Purdy, RW Peterson, PL Yu, and CA Regal. Cavity optomechanics with Si_3N_4 membranes at cryogenic temperatures. *New Journal of Physics*, 14(11):115021, 2012.
- [47] Thomas Gisler, Mohamed Helal, Deividus Sabonis, Urs Grob, Martin Hérítier, Christian L Degen, Amir H Ghadimi, and Alexander Eichler. Soft-clamped silicon nitride string resonators at millikelvin temperatures. *Physical Review Letters*, 129(10):104301, 2022.
- [48] JD Thompson, BM Zwickl, AM Jayich, Florian Marquardt, SM Girvin, and JGE Harris. Strong dispersive coupling of a high-finesse cavity to a micromechanical membrane. *Nature*, 452(7183):72–75, 2008.
- [49] Tom P Purdy, Robert W Peterson, and CA Regal. Observation of radiation pressure shot noise on a macroscopic object. *Science*, 339(6121):801–804, 2013.
- [50] Massimiliano Rossi, David Mason, Junxin Chen, Yeghishe Tsaturyan, and Albert Schliesser. Measurement-based quantum control of mechanical motion. *Nature*, 563(7729):53–58, 2018.
- [51] Junxin Chen, Massimiliano Rossi, David Mason, and Albert Schliesser. Entanglement of propagating optical modes via a mechanical interface. *Nature communications*, 11(1):943, 2020.
- [52] Thomas P Purdy, P-L Yu, Robert W Peterson, Nir S Kampel, and Cindy A Regal. Strong optomechanical squeezing of light. *Physical Review X*, 3(3):031012, 2013.
- [53] Reed W Andrews, Robert W Peterson, Tom P Purdy, Katarina Cicak, Raymond W Simmonds, Cindy A Regal, and Konrad W Lehnert. Bidirectional and efficient conversion between microwave and optical light. *Nature physics*, 10(4):321–326, 2014.
- [54] Mads Bjerregaard Kristensen, Nenad Kralj, Eric C Langman, and Albert Schliesser. Long-lived and efficient optomechanical memory for light. *Physical Review Letters*, 132(10):100802, 2024.
- [55] Mario F Gely and Gary A Steele. Superconducting electro-mechanics to test diósi–penrose effects of general relativity in massive superpositions. *AVS Quantum Science*, 3(3), 2021.
- [56] Jack Manley, Mitul Dey Chowdhury, Daniel Grin, Swati Singh, and Dalziel J Wilson. Searching for vector dark matter with an optomechanical accelerometer. *Physical review letters*, 126(6):061301, 2021.
- [57] David Mason, Junxin Chen, Massimiliano Rossi, Yeghishe Tsaturyan, and Albert Schliesser. Continuous force and displacement measurement below the standard quantum limit. *Nature Physics*, 15(8):745–749, 2019.
- [58] Johannes M Fink, Mahmoud Kalaei, Alessandro Pitanti, Richard Norte, Lukas Heinzle, Marcelo Davanço, Kartik Srinivasan, and Oskar Painter. Quantum electromechanics on silicon nitride nanomembranes. *Nature communications*, 7(1):12396, 2016.
- [59] Nikaya Snell, Chang Zhang, Gengyang Mu, Alexandre Bouchard, and Raphael St-Gelais. Heat transport in silicon nitride drum resonators and its influence on thermal fluctuation-induced frequency noise. *Physical Review Applied*, 17(4):044019, 2022.
- [60] Fan Yang, Felix Rochau, Jana S Huber, Alexandre Brioussel, Gianluca Rastelli, Eva M Weig, and Elke Scheer. Spatial modulation of nonlinear flexural vibrations of membrane resonators. *Physical review letters*, 122(15):154301, 2019.
- [61] Keivan Asadi, Jun Yu, and Hanna Cho. Nonlinear couplings and energy transfers in micro-and nanomechanical resonators: intermodal coupling, internal resonance and synchronization. *Philosophical Transactions of the Royal Society A: Mathematical, Physical and Engineering Sciences*, 376(2127):20170141, 2018.
- [62] Luis Mestre, Suyash Singh, Gabriel Margiani, Letizia Catalini, Alexander Eichler, and Vincent Dumont. Network of parametrically driven silicon nitride mechanical membranes. *Physical Review Applied*, 24(4):044072, 2025.
- [63] Parmeshwar Prasad, Nishta Arora, and AK Naik. Gate tunable cooperativity between vibrational modes. *Nano Letters*, 19(9):5862–5867, 2019.
- [64] Zichao Li, Minxing Xu, Richard A Norte, Alejandro M Aragón, Peter G Steeneken, and Farbod Alijani. Cascade of modal interactions in nanomechanical resonators with soft clamping. *arXiv preprint arXiv:2507.00805*, 2025.
- [65] Nishta Arora and Akshay K Naik. Qualitative effect of internal resonance on the dynamics of two-dimensional resonator. *Journal of Physics D: Applied Physics*, 55(26):265301, 2022.
- [66] Nishta Arora, Priyanka Singh, Randhir Kumar, Rudra Pratap, and Akshay Naik. Mixed nonlinear response and transition of nonlinearity in a piezoelectric membrane. *ACS Applied Electronic Materials*, 6(1):155–162, 2024.
- [67] Johannes Güttinger, Adrien Noury, Peter Weber, Axel Martin Eriksson, Camille Lagoin, Joel Moser, Christopher Eichler, Andreas Wallraff, Andreas Isacsson, and Adrian Bachtold. Energy-dependent path of dissipation in nanomechanical resonators. *Nature nanotechnology*, 12(7):631–636, 2017.
- [68] Ata Keşkekler, Oriël Shoshani, Martin Lee, Herre SJ van der Zant, Peter G Steeneken, and Farbod Alijani. Tuning nonlinear damping in graphene nanoresonators by parametric–direct internal resonance. *Nature communications*, 12(1):1099, 2021.
- [69] Parmeshwar Prasad, Nishta Arora, and AK Naik. Tunable nonlinear damping in MoS_2 nanoresonator. *Applied Physics Letters*, 123(26), 2023.
- [70] Arthur W Leissa. *Vibration of plates*, volume 160. Scientific and Technical Information Division, National Aeronautics and Space Administration, 1969.

- [71] Gregory William Vogl. Nonlinear dynamics of circular plates under electrical loadings for capacitive micromachined ultrasonic transducers (cmuts). 2006.
- [72] Chandan Samanta, Nishta Arora, and AK Naik. Tuning of geometric nonlinearity in ultrathin nanoelectromechanical systems. *Applied Physics Letters*, 113(11), 2018.
- [73] William Hvidtfelt Padkær Nielsen, Yeghishe Tsaturyan, Christoffer Bo Møller, Eugene S Polzik, and Albert Schliesser. Multimode optomechanical system in the quantum regime. *Proceedings of the National Academy of Sciences*, 114(1):62–66, 2017.
- [74] Chao Meng, George A Brawley, Soroush Khademi, Elizabeth M Bridge, James S Bennett, and Warwick P Bowen. Measurement-based preparation of multimode mechanical states. *Science Advances*, 8(21):eabm7585, 2022.
- [75] Han Zhao, William David Chen, Abhishek Kejriwal, and Mohammad Mirhosseini. Quantum-enabled microwave-to-optical transduction via silicon nanomechanics. *Nature Nanotechnology*, pages 1–7, 2025.

* These authors contributed equally to this work.

† Corresponding author: nishta@iisc.ac.in
 ‡ Corresponding author: csamanta@iiserb.ac.in

Acknowledgments

A.N. acknowledges funding support from MHRD, MeitY and DST Nano Mission through NNetRA. N.A. acknowledges fellowship support under Visvesvaraya Ph.D. Scheme, Ministry of Electronics and Information Technology (MeitY), India. C.S. acknowledges financial support from the Anusandhan National Research Foundation (ANRF), India, under Project No. ANRF/ECRG/2024/006637/PMS.

Competing Interests

The authors declare no competing interests.

Supplementary Information for Nonlinear Mode Coupling in Silicon Nitride Membrane Resonators

Soumya Kanti Das,^{1,*} Nishta Arora,^{2,*} Hridhay A S,¹ Akshay Naik,² Chandan Samanta¹

¹Department of Physics,

Indian Institute of Science Education and Research Bhopal, Bhopal-462066, Madhya Pradesh, India

²Centre for Nano Science and Engineering,

Indian Institute of Science, Bengaluru-560012, Karnataka, India

Contents

| | | |
|----------|--|----------|
| 1 | Theoretical description | 1 |
| 1.1 | Duffing nonlinearity | 1 |
| 1.2 | Nonlinear mode coupling | 4 |
| 1.3 | Nonlinear frequency pulling | 6 |
| 2 | Experimental Section | 7 |
| 2.1 | Device parameters | 7 |
| 2.2 | Displacement calibration | 8 |
| 2.3 | Frequency responses of modes (2, 1) and (2, 2) | 8 |

1 Theoretical description

We model nonlinear mode coupling behavior of a square silicon nitride (Si_3N_4) membrane resonator using Kirchhoff–Love plate theory. We first analyze the intramode coupling (intrinsic Duffing nonlinearity) of the resonator and then introduce intermodal mode-coupling terms to develop a general coupling framework. The Duffing constants and a general expression for the coupling constant between probing mode (n, m) and driving mode (p, q) are derived. The theoretical results show good agreement with experimental observations.

1.1 Duffing nonlinearity

With the use of Kirchhoff-Love plate theory[1], the general equation characterizing the transverse displacement $w(x, y, t)$ of a thin plate can be written as

$$D\nabla^4 w(x, y, t) - \left(N_{xx} \frac{\partial^2 w}{\partial x^2} + 2N_{xy} \frac{\partial^2 w}{\partial x \partial y} + N_{yy} \frac{\partial^2 w}{\partial y^2} \right) + \rho h \frac{\partial^2 w}{\partial t^2} = 0 \quad (S1)$$

where $w(x, y, t) = \phi(x, y) z(t) = \sin(\frac{n\pi x}{L}) \sin(\frac{m\pi y}{L}) z(t)$, D is the flexural rigidity, N_{xx} , N_{yy} , and N_{xy} are the in-plane stress resultants, which can be defined as

$$N_{xx} = \int_{-h/2}^{h/2} \sigma_{xx} dz, \quad (\text{S2})$$

$$N_{yy} = \int_{-h/2}^{h/2} \sigma_{yy} dz, \quad (\text{S3})$$

$$N_{xy} = \int_{-h/2}^{h/2} \sigma_{xy} dz, \quad (\text{S4})$$

here, σ_{xx} , σ_{yy} and σ_{xy} is defined as

$$\sigma_{xx} = \frac{E}{1 - \nu^2} (\epsilon_{xx} + \nu \epsilon_{yy}), \quad (\text{S5})$$

$$\sigma_{yy} = \frac{E}{1 - \nu^2} (\epsilon_{yy} + \nu \epsilon_{xx}), \quad (\text{S6})$$

$$\sigma_{xy} = \frac{E}{1 + \nu} \epsilon_{xy}. \quad (\text{S7})$$

Due to the thinness of our membrane, we assume that the Poisson's ratio (ν) is zero. In the presence of nonlinear displacement, particularly due to geometrical nonlinearity, the strain components are defined as [2]

$$\epsilon_{xx} = \epsilon_0 + \frac{\partial u_0}{\partial x} + \frac{1}{2} \left(\frac{\partial w}{\partial x} \right)^2 - z(t) \frac{\partial^2 w}{\partial x^2}, \quad (\text{S8})$$

$$\epsilon_{yy} = \epsilon_0 + \frac{\partial v_0}{\partial y} + \frac{1}{2} \left(\frac{\partial w}{\partial y} \right)^2 - z(t) \frac{\partial^2 w}{\partial y^2}, \quad (\text{S9})$$

$$\epsilon_{xy} = \frac{1}{2} \left(\frac{\partial u_0}{\partial y} + \frac{\partial v_0}{\partial x} \right) + \frac{1}{2} \frac{\partial w}{\partial x} \frac{\partial w}{\partial y} - z(t) \frac{\partial^2 w}{\partial x \partial y}. \quad (\text{S10})$$

For a thin membrane, we assume that in-plane mid-surface displacements are minimal, namely $u_0, v_0 = 0$, and that in-plane displacements resulting from transverse deformation are insignificant. With these assumptions, the stress resultants are simplified to

$$N_{xx} = Eh \left(\epsilon_0 + \frac{1}{2} \left(\frac{\partial w}{\partial x} \right)^2 \right), \quad (\text{S11})$$

$$N_{yy} = Eh \left(\epsilon_0 + \frac{1}{2} \left(\frac{\partial w}{\partial y} \right)^2 \right), \quad (\text{S12})$$

$$N_{xy} = \frac{1}{2} Eh \left(\frac{\partial w}{\partial x} \frac{\partial w}{\partial y} \right). \quad (\text{S13})$$

Substituting into the governing equation (S1) and employing the Galerkin method with $w(x, y, t) = \sin(\frac{n\pi x}{L}) \sin(\frac{m\pi y}{L}) z(t)$, also neglecting D for the high-stress scenario [3], we obtain

$$\begin{aligned} & - \int_0^L \int_0^L \left(N_{xx} \frac{\partial^2 w}{\partial x^2} + 2N_{xy} \frac{\partial^2 w}{\partial x \partial y} + N_{yy} \frac{\partial^2 w}{\partial y^2} \right) \phi(x, y) dx dy \\ & + \rho h \int_0^L \int_0^L \frac{\partial^2 w}{\partial t^2} \phi(x, y) dx dy = 0 \end{aligned} \quad (\text{S14})$$

The expressions for N_{xx} , N_{yy} , and N_{xy} becomes

$$N_{xx} = Eh \left[\epsilon_0 + \frac{1}{2}z^2(t) \left(\frac{n\pi}{L} \right)^2 \sin^2 \left(\frac{m\pi y}{L} \right) \times \cos^2 \left(\frac{n\pi x}{L} \right) \right], \quad (\text{S15})$$

$$N_{yy} = Eh \left[\epsilon_0 + \frac{1}{2}z^2(t) \left(\frac{m\pi}{L} \right)^2 \sin^2 \left(\frac{n\pi x}{L} \right) \times \cos^2 \left(\frac{m\pi y}{L} \right) \right], \quad (\text{S16})$$

$$N_{xy} = \frac{1}{2}Ehz^2(t) \left(\frac{n\pi}{L} \right) \left(\frac{m\pi}{L} \right) \times \sin \left(\frac{n\pi x}{L} \right) \cos \left(\frac{n\pi x}{L} \right) \sin \left(\frac{m\pi y}{L} \right) \cos \left(\frac{m\pi y}{L} \right). \quad (\text{S17})$$

Upon substituting into equation (S14), we can find the integrals

$$K_1 = \int_0^L \int_0^L N_{xx} \frac{\partial^2 w}{\partial x^2} \phi(x, y) dx dy \quad (\text{S18})$$

$$K_2 = \int_0^L \int_0^L N_{yy} \frac{\partial^2 w}{\partial y^2} \phi(x, y) dx dy \quad (\text{S19})$$

$$K_3 = \int_0^L \int_0^L 2N_{xy} \frac{\partial^2 w}{\partial x \partial y} \phi(x, y) dx dy \quad (\text{S20})$$

By solving the integral and substituting these values into Eq. (S14), we have derived the equation

$$\rho h \frac{L^2}{4} \frac{d^2 z}{dt^2} + Eh\epsilon_0 \frac{L^2}{4} \left(\frac{\pi}{L} \right)^2 (n^2 + m^2)z(t) + \frac{3}{2}Eh \frac{L^2}{64} \left(\frac{\pi}{L} \right)^4 \left[n^4 + m^4 - \frac{2}{3}n^2m^2 \right] z^3(t) = 0 \quad (\text{S21})$$

From there we can find,

$$\omega_{nm}^2 = \frac{E\epsilon_0\pi^2(n^2 + m^2)}{\rho L^2} \quad (\text{S22})$$

And,

$$\alpha_{nm} = \frac{3E}{32\rho} \left(\frac{\pi}{L} \right)^4 \left[n^4 + m^4 - \frac{2}{3}n^2m^2 \right] \quad (\text{S23})$$

To determine the resonant frequency and the Duffing nonlinearity, we employed Eq.(S21); however, a damping component and a driving force term will typically be present as well. To analyze the nonlinear response, it is essential to include the driving force term, as outlined in the paper. The equation of motion, incorporating both the driving force and damping terms, can be expressed as

$$\frac{d^2 z}{dt^2} + \nu \frac{dz}{dt} + \omega_{nm}^2 z + \alpha_{nm} z^3 = f_d \cos(\omega t) \quad (\text{S24})$$

here, ν represents the damping factor, while $f_d \cos(\omega t)$ denotes the driving force. The driving force is either high or low, as indicated by the driving force amplitude f_d .

1.2 Nonlinear mode coupling

We have not previously looked at the mode coupling term. The in-plane tension can be adjusted for mode coupling. Considering non-linear mode coupling, the values of ϵ_{xx} , ϵ_{yy} , ϵ_{xy} will be

$$\epsilon_{xx} = \frac{\partial u_0}{\partial x} + \frac{1}{2} \left[\left(\frac{\partial w_1}{\partial x} \right)^2 + \left(\frac{\partial w_2}{\partial x} \right)^2 \right] - z_1(t) \frac{\partial^2 w_1}{\partial x^2} \quad (\text{S25})$$

$$\epsilon_{yy} = \frac{\partial v_0}{\partial y} + \frac{1}{2} \left[\left(\frac{\partial w_1}{\partial y} \right)^2 + \left(\frac{\partial w_2}{\partial y} \right)^2 \right] - z_1(t) \frac{\partial^2 w_1}{\partial y^2} \quad (\text{S26})$$

$$\epsilon_{xy} = \frac{1}{2} \left(\frac{\partial u_0}{\partial y} + \frac{\partial v_0}{\partial x} \right) + \frac{1}{2} \left[\left(\frac{\partial w_1}{\partial x} \frac{\partial w_1}{\partial y} \right) + \left(\frac{\partial w_2}{\partial x} \frac{\partial w_2}{\partial y} \right) \right] - z_1(t) \frac{\partial^2 w_1}{\partial x \partial y} \quad (\text{S27})$$

Here, $w_1 = \phi_1(x, y)z_1(t) = \sin\left(\frac{n\pi x}{L}\right) \sin\left(\frac{m\pi y}{L}\right) z_1(t)$, where (n, m) denotes the mode number of the probe mode, and $w_2 = \phi_2(x, y)z_2(t) = \sin\left(\frac{p\pi x}{L}\right) \sin\left(\frac{q\pi y}{L}\right) z_2(t)$, where (p, q) signifies the mode number corresponding to the pump mode. Once more, we can apply the aforementioned thin membrane approximation. The in-plane stress resultants can now be expressed as

$$N_{xx} = Eh \left[\epsilon_0 + \frac{1}{2} \left\{ \left(\frac{\partial w_1}{\partial x} \right)^2 + \left(\frac{\partial w_2}{\partial x} \right)^2 \right\} \right] \quad (\text{S28})$$

$$N_{yy} = Eh \left[\epsilon_0 + \frac{1}{2} \left\{ \left(\frac{\partial w_1}{\partial y} \right)^2 + \left(\frac{\partial w_2}{\partial y} \right)^2 \right\} \right] \quad (\text{S29})$$

$$N_{xy} = \frac{1}{2} Eh \left[\left(\frac{\partial w_1}{\partial x} \frac{\partial w_1}{\partial y} \right) + \left(\frac{\partial w_2}{\partial x} \frac{\partial w_2}{\partial y} \right) \right] \quad (\text{S30})$$

The contributions to the mode coupling factor from the terms N_{xx} , N_{yy} , N_{xy} are as follows

$$N_{xx,\lambda} = \frac{Eh}{2} \left(\frac{\partial w_2}{\partial x} \right)^2 \quad (\text{S31})$$

$$N_{yy,\lambda} = \frac{Eh}{2} \left(\frac{\partial w_2}{\partial y} \right)^2 \quad (\text{S32})$$

$$N_{xy,\lambda} = \frac{Eh}{2} \left(\frac{\partial w_2}{\partial x} \frac{\partial w_2}{\partial y} \right) \quad (\text{S33})$$

Substituting the values of w_2 yields

$$N_{xx,\lambda} = \frac{Eh}{2} \left[\left(\frac{p\pi}{L} \right)^2 \cos^2 \left(\frac{p\pi x}{L} \right) \sin^2 \left(\frac{q\pi y}{L} \right) \right] \quad (\text{S34})$$

$$N_{yy,\lambda} = \frac{Eh}{2} \left[\left(\frac{q\pi}{L} \right)^2 \sin^2 \left(\frac{p\pi x}{L} \right) \cos^2 \left(\frac{q\pi y}{L} \right) \right] \quad (\text{S35})$$

$$N_{xy,\lambda} = \frac{1}{2} Eh \left[\left(\frac{p\pi}{L} \right) \cos \left(\frac{p\pi x}{L} \right) \sin \left(\frac{q\pi y}{L} \right) \left(\frac{q\pi}{L} \right) \sin \left(\frac{p\pi x}{L} \right) \cos \left(\frac{q\pi y}{L} \right) \right] \quad (\text{S36})$$

To calculate the coupling constant, it is necessary to solve the integrals

$$\int_0^L \int_0^L N_{xx,\lambda} \frac{\partial^2 w_1}{\partial x^2} \phi_1(x, y) dx dy \quad (\text{S37})$$

$$\int_0^L \int_0^L N_{yy,\lambda} \frac{\partial^2 w_1}{\partial y^2} \phi_1(x, y) dx dy \quad (\text{S38})$$

$$\int_0^L \int_0^L 2N_{xy,\lambda} \frac{\partial^2 w_1}{\partial x \partial y} \phi_1(x, y) dx dy \quad (\text{S39})$$

The expression for coupling constant is

$$\lambda_{nm}^{pq} = \frac{-\int_0^L \int_0^L \left(N_{xx,\lambda} \frac{\partial^2 w_1}{\partial x^2} \phi_1(x, y) + N_{yy,\lambda} \frac{\partial^2 w_1}{\partial y^2} \phi_1(x, y) + 2N_{xy,\lambda} \frac{\partial^2 w_1}{\partial x \partial y} \phi_1(x, y) \right) dx dy}{\rho h \left(\frac{L^2}{4} \right)} \quad (\text{S40})$$

Where the denominator comes from Eq.(S21). Considering the mode number (p, q) , where $p = q > 1$, when coupled with mode $(1,1)$, the expression for the coupling constant can be defined as

$$\lambda_{11}^{pq} = \frac{E}{8\rho} \left(\frac{\pi}{L} \right)^4 [p^2 + q^2] \quad (\text{S41})$$

We have derived an equation similar to (S24) that includes the mode coupling term. The equation may be expressed as

$$\frac{d^2 z_1}{dt^2} + \nu_1 \frac{dz_1}{dt} + \omega_{nm}^2 z_1 + \alpha_{nm} z_1^3 + \lambda_{nm}^{pq} z_1 z_2^2 = f_p \cos(\omega t) \quad (\text{S42})$$

This equation represents the mode coupling of the probe mode, which exhibits displacement along the z axis (z_1), with the driving mode, whose displacement is z_2 . ν_1 , ω_{nm} , α_{nm} , and λ_{nm}^{pq} represent the damping constant, natural frequency, Duffing constant of the probe mode, respectively and λ_{nm}^{pq} is the coupling constant between probe mode (n, m) and drive mode (p, q) . We have numerically determined the coupling constant using Equation (S40). When $p = n$ and $q = m$, the coupling constant λ_{pq}^{nm} reduces to α_{nm} , corresponding to the intramode coupling, which is basically the Duffing constant.

Table 1: Coupling constant for unit modal mass for mode (p, q) , where p, q runs from 1 to 5, coupled with $(2,2)$ mode. The values of the coupling constant are of the order $10^{23} m^{-2} s^{-2}$. The intramode coupling constant (Duffing constant) is highlighted in blue.

| | $q = 1$ | $q = 2$ | $q = 3$ | $q = 4$ | $q = 5$ |
|---------|---------|-------------|---------|---------|---------|
| $p = 1$ | 1.38 | 2.41 | 6.88 | 11.70 | 17.89 |
| $p = 2$ | 2.41 | 2.75 | 10.67 | 17.89 | 27.19 |
| $p = 3$ | 6.88 | 10.67 | 12.39 | 17.21 | 23.40 |
| $p = 4$ | 11.70 | 17.89 | 17.21 | 22.03 | 28.22 |
| $p = 5$ | 17.89 | 27.19 | 23.40 | 28.22 | 34.42 |

Table 2: Coupling constant for unit modal mass for mode (p, q) , where p, q runs from 1 to 5, coupled with $(3,3)$ mode. The values of the coupling constant are of the order $10^{23} m^{-2} s^{-2}$. The intramode coupling constant (Duffing constant) is highlighted in blue.

| | $q = 1$ | $q = 2$ | $q = 3$ | $q = 4$ | $q = 5$ |
|---------|---------|---------|--------------|---------|---------|
| $p = 1$ | 3.09 | 7.74 | 9.29 | 26.33 | 40.27 |
| $p = 2$ | 7.74 | 12.39 | 16.26 | 30.97 | 44.91 |
| $p = 3$ | 9.29 | 16.26 | 13.93 | 44.14 | 65.05 |
| $p = 4$ | 26.33 | 30.97 | 44.14 | 53.60 | 63.50 |
| $p = 5$ | 40.27 | 44.91 | 65.05 | 63.60 | 77.44 |

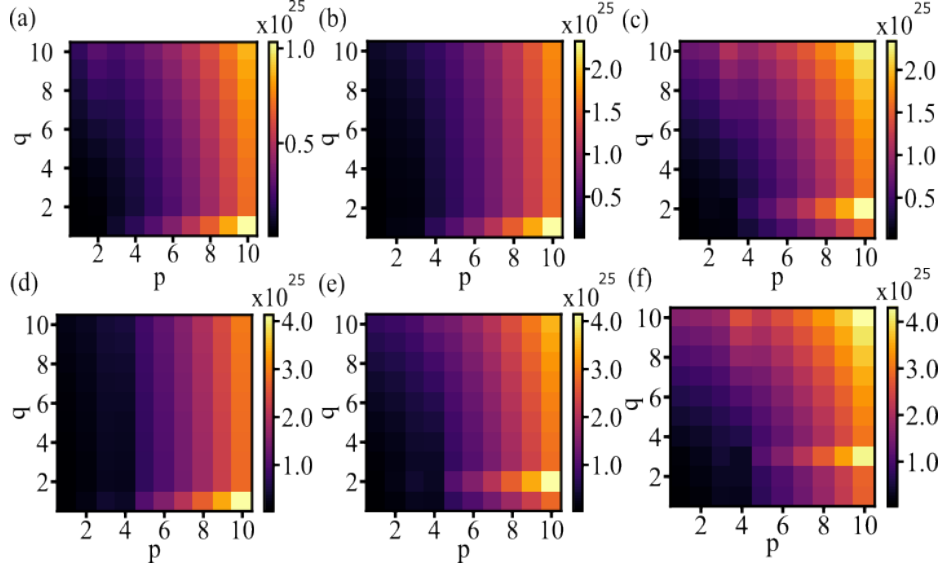


Fig. S1: Theoretical estimation of the nonlinear mode coupling matrix. (a–f) Calculated coupling constants as a function of the driven mode indices (p, q) for $p, q = 1-10$, coupled to the probe modes $(2, 1)$, $(3, 1)$, $(3, 2)$, $(4, 1)$, $(4, 2)$ and $(4, 3)$, respectively.

1.3 Nonlinear frequency pulling

The frequency detuning equation for mode coupling is derived using the method of multiple scales[4]. This approach alters the time scale as follows

$$T_n = \epsilon^n t, \quad (\text{S43})$$

where $T_0 = t$, and ϵ is the scaling parameter. For using method of multiple scale the Eq (S42) can be modified as

$$\ddot{z}_1 + 2\epsilon\mu_1\dot{z}_1 + \omega_{nm}^2 z_1 + \epsilon\alpha_{nm}z_1^3 + \epsilon\lambda_{nm}^{pq}z_1z_2^2 = \epsilon k_d \cos(\omega_{nm}T_0 + \sigma T_1). \quad (\text{S44})$$

Using the method of multiple scale method we have reached a equation as

$$\sigma = \frac{3\alpha_{nm}}{8\omega_{nm}}(z_1^{peak})^2 \pm \sqrt{\frac{k_d^2}{4\omega_{nm}^2(z_1^{peak})^2} - \mu_1^2} + \frac{\lambda_{nm}^{pq}}{2\omega_{nm}}z_2^2. \quad (\text{S45})$$

For steady state the middle term in the RHS becomes zero. Then we can get a equation like

$$\sigma = \frac{3\alpha_{nm}}{8\omega_{nm}}(z_1^{peak})^2 + \frac{\lambda_{nm}^{pq}}{2\omega_{nm}}z_2^2. \quad (\text{S46})$$

Here, $\sigma = \omega - \omega_{nm}$ denotes the frequency detuning. This equation represents the frequency detuning generated by mode coupling, enabling the determination of the coupling constant (λ_{nm}^{pq}). In the absence of mode coupling, the equation assumes the following form

$$\sigma = \frac{3\alpha_{nm}}{8\omega_{nm}}(z_1^{peak})^2. \quad (\text{S47})$$

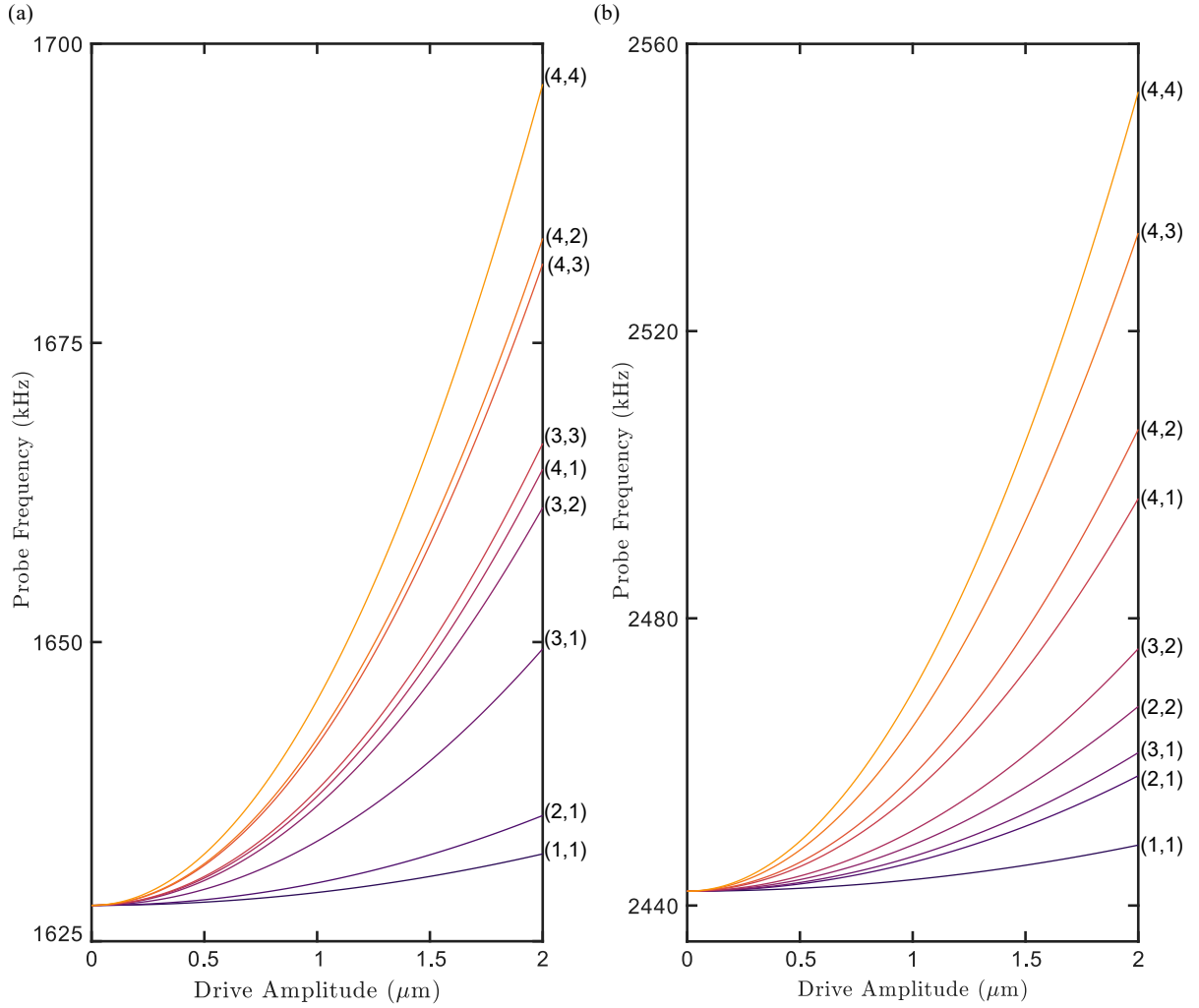


Fig. S2: Predicted frequency shift of the fundamental mode (a)(2,2), (b)(3,3) as a function of the coupled-mode amplitude.

Equation (S47) helps us for the calculation of the experimental Duffing constant (α_{nm}). When the applied force is sufficiently small, the nonlinear terms in Eq. (S45) can be neglected. Using the coupling constant, the resulting shift in the resonance frequency of the probe mode can then be plotted as a function of the drive-mode amplitude. The resonance-frequency shifts of the (2,2) and (3,3) modes as functions of the peak amplitudes of the other coupled modes are shown in Fig. S2. The graph illustrates the extent of the change in resonant frequency of the modes that can occur when the coupled mode possesses the specified amplitude.

2 Experimental Section

2.1 Device parameters

The device parameters used in this work are summarized in Table 3. The strain is calculated using the resonance frequency relation given in Eq.(S22). Using the extracted strain and the Young's modulus, the corresponding tensile stress is estimated to be approximately 1.05 GPa, consistent with previously reported values [5].

| Physical Parameter | Value |
|---------------------------------|---------------------------|
| Young's Modulus (E) | 280×10^9 Pa |
| Density (ρ) | 3170 kg/m^3 [6] |
| Inbuilt Strain (ϵ_0) | 3.751×10^{-3} |
| Length (L) | 500×10^{-6} m |
| Thickness (h) | 100×10^{-9} m |

Table 3: Device Parameters

2.2 Displacement calibration

The displacement of the membrane was calibrated using the laser Doppler vibrometer (LDV), which provides an absolute measurement of the out-of-plane displacement. To establish a conversion between the electrical readout voltage and the physical displacement, the device was driven with a low-frequency sinusoidal excitation of known amplitude while simultaneously recording the displacement using the LDV and the corresponding voltage signal using the lock-in amplifier. Figure S3 shows the measured displacement as a function of the detected voltage. A linear fit to the data yields a calibration factor of $\frac{\partial z}{\partial V} = 0.2 \mu\text{m/V}$, where z is the mechanical displacement and V is the measured voltage at the lock-in amplifier.

This calibration factor was subsequently used to convert all voltage signals measured using the lock-in amplifier into absolute displacement units. Specifically, the displacement amplitude was obtained as $z(t) = \alpha V(t)$, where $\alpha = 0.2 \mu\text{m/V}$ is the experimentally determined conversion factor. Since the LDV provides an absolute displacement reference traceable to optical wavelength standards, this procedure enables quantitative displacement measurements without reliance on device parameters.

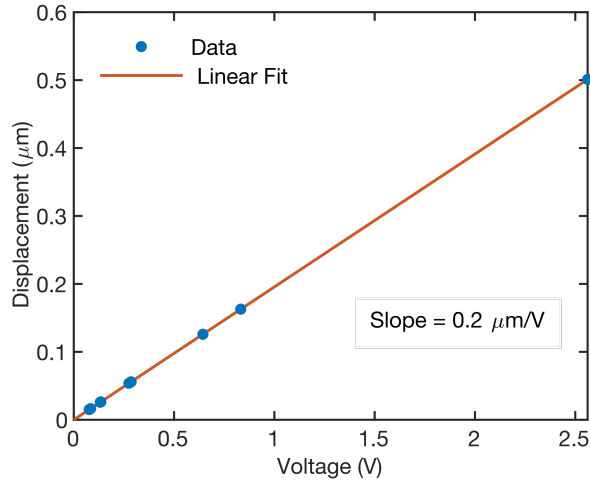


Fig. S3: Measured mechanical displacement z as a function of the detected lock-in amplifier voltage V . A linear fit to the data yields a displacement calibration factor of $\partial z/\partial V = 0.2 \mu\text{m V}^{-1}$.

2.3 Frequency responses of modes (2, 1) and (2, 2)

Figures S4(b,e) show the linear frequency responses of the (2, 1) and (2, 2) modes respectively. The solid lines represent Lorentzian fits to the data, yielding quality factors of 12.5×10^4 for the (2, 1)

mode and 11.5×10^4 for the mode (2, 2). As the driving force is increased, the frequency response becomes progressively nonlinear, as illustrated in Figs. S4(a,d). Figures S4(c,f) show the extracted frequency shift as a function of the peak amplitudes. The solid lines correspond to fits using Eq. (S47), from which the experimental Duffing coefficients are obtained to be $2.5 \times 10^{23} \text{ m}^{-2}\text{s}^{-2}$ and $4.7 \times 10^{23} \text{ m}^{-2}\text{s}^{-2}$ for mode (2, 1) and (2, 2) respectively.

Throughout the measurements, the LDV laser spot was fixed at the center of the membrane. This position corresponds to the anti-node of the (1,1) mode but lies close to the nodal regions of the higher-order (2,1) and (2,2) modes. As a result, the measured displacement amplitudes for these modes are small, leading to increased amplitude fluctuations, as observed in Fig. S4(a,d). To account for this effect, scaling factors were estimated from the extrema of the spatial mode shapes shown in Fig. 1 in the main text. The scaling factor is 10.2 ± 4.0 for the (2,1) mode and 25.2 ± 11.0 for the (2,2) mode. The uncertainty arises from the mismatch between the LDV laser spot size ($\sim 1 \mu\text{m}$) and the step size used in the mode-shape measurements ($\sim 50 \mu\text{m}$). In addition, the localized peak near $\sim 1628 \text{ kHz}$ is attributed to higher-harmonic contributions from the parametrically driven fundamental mode.

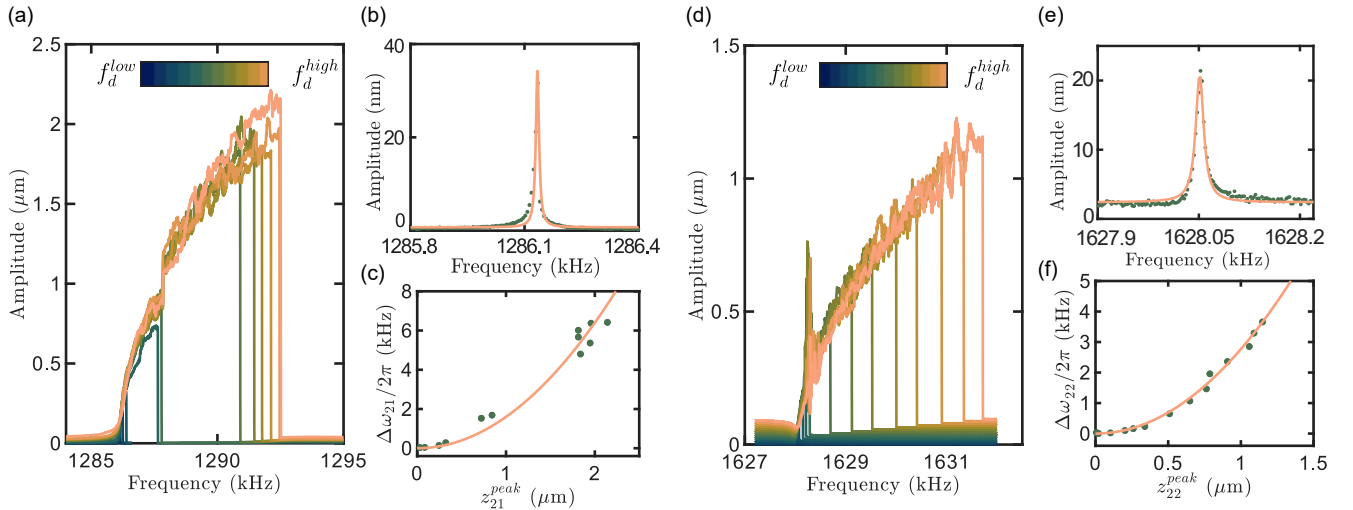


Fig. S4: (a,d) Nonlinear frequency responses of mode (2, 1) and (2, 2) at increasing driving force. (b,e) Linear responses of the (2, 1) and (2, 2) modes at the lowest drive amplitudes; solid lines indicate Lorentzian fits used to extract the resonance frequencies and quality factors. (c,f) Amplitude-dependent frequency shifts corresponding to the maximum displacement amplitudes extracted from (a,d). Solid lines show fits to extract the Duffing coefficients.

References

- [1] Arthur W Leissa. *Vibration of plates*. Vol. 160. Scientific, Technical Information Division, National Aeronautics, and Space Administration, 1969.
- [2] E Ventsel, T Krauthammer, and E Carrera. *Thin plates and shells: theory, analysis, and applications*. 2002.
- [3] D Cattiaux et al. “Geometrical nonlinearity of circular plates and membranes: An alternative method”. In: *Journal of Applied Physics* 128.10 (2020).
- [4] Inna Kozinsky. “Nonlinear nanoelectromechanical systems”. In: *Ph. D. Thesis* (2007).

- [5] Bin Shu et al. “Fabrication of high compressive stress silicon nitride membrane in strained silicon technology”. In: *2009 IEEE International Conference of Electron Devices and Solid-State Circuits (EDSSC)*. IEEE. 2009, pp. 365–367.
- [6] Luis Mestre et al. “Network of parametrically driven silicon nitride mechanical membranes”. In: *Physical Review Applied* 24.4 (2025), p. 044072.